

RESEARCH ARTICLE

10.1002/2016JB013365

Key Points:

- Fluid viscosity affects HF process and induced crack properties
- Low-viscosity fracturing fluid tends to induce sinuous cracks with many branches
- CO₂ fracturing most likely makes pathways favorable for EGS

Supporting Information:

- Figures S1–S3
- Table S1
- Table S2
- Table S3
- Table S4

Correspondence to:

T. Ishida,
ishida.tsuyoshi.2a@kyoto-u.ac.jp

Citation:

Ishida, T., Y. Chen, Z. Bennour, H. Yamashita, S. Inui, Y. Nagaya, M. Naoi, Q. Chen, Y. Nakayama, and Y. Nagano (2016), Features of CO₂ fracturing deduced from acoustic emission and microscopy in laboratory experiments, *J. Geophys. Res. Solid Earth*, 121, 8080–8098, doi:10.1002/2016JB013365.

Received 19 JUL 2016

Accepted 17 OCT 2016

Accepted article online 18 OCT 2016

Published online 11 NOV 2016

Features of CO₂ fracturing deduced from acoustic emission and microscopy in laboratory experiments

Tsuyoshi Ishida¹, Youqing Chen², Ziad Bennour¹, Hiroto Yamashita¹, Shuhei Inui¹, Yuya Nagaya¹, Makoto Naoi¹, Qu Chen³, Yoshiki Nakayama³, and Yu Nagano⁴
¹Department of Civil and Earth Resources Engineering, Graduate School of Engineering, Kyoto University, Kyoto, Japan,

²Department of Energy Science and Technology, Graduate School of Energy Science, Kyoto University, Kyoto, Japan, ³3D Geoscience, Inc., Tokyo, Japan, ⁴Japan Oil, Gas and Metals National Corporation, Chiba, Japan

Abstract We conducted hydraulic fracturing (HF) experiments on 170 mm cubic granite specimens with a 20 mm diameter central hole to investigate how fluid viscosity affects HF process and crack properties. In experiments using supercritical carbon dioxide (SC-CO₂), liquid carbon dioxide (L-CO₂), water, and viscous oil with viscosity of 0.051–336.6 mPa · s, we compared the results for breakdown pressure, the distribution and fracturing mechanism of acoustic emission, and the microstructure of induced cracks revealed by using an acrylic resin containing a fluorescent compound. Fracturing with low-viscosity fluid induced three-dimensionally sinuous cracks with many secondary branches, which seem to be desirable pathways for enhanced geothermal system, shale gas recovery, and other processes.

1. Introduction

The underground sequestration of carbon dioxide (CO₂) is a promising and feasible method for mitigating the greenhouse effect by decreasing the amount of CO₂ emissions. If this method can offer economic benefits to compensate for the costs of the capture, transportation, and underground injection of CO₂, it will be much more eagerly developed and adopted.

Brown [2000] proposed to use CO₂ instead of water to extract heat from enhanced geothermal system (EGS) with realizing the underground sequestration of CO₂ at the same time. Ueda *et al.* [2005] suggested that CO₂ injected through a borehole can be dissolved into groundwater and the CO₂-saturated water reacts with the hot rocks to form calcite and clay minerals at the edge of the migrating plume of CO₂. An impermeable layer composed of the calcite and the clay minerals can act as a cap rock to retain CO₂. Pruett [2006] compared the flow behavior, chemistry, and thermophysical properties of CO₂ and water for geothermal energy extraction and concluded that CO₂ is superior to water as a working fluid for EGS. Mohan *et al.* [2013] explored the possibility of utilizing CO₂ as alternative geothermal fluid for the extraction of geothermal heat in arid regions and to simultaneously sequester CO₂. Xu *et al.* [2016] assessed the power generation and CO₂ sequestration ability of the Habanero geothermal field in the Cooper Basin of South Australia and suggested through their simulation that the major sequestration mechanisms are the storage in the fracture-stimulation damage zone.

Injection to extract heat energy from EGS is usually injected into rock masses at a depth of more than 3000 m, which satisfy the temperature and the pressure to make CO₂ supercritical state. The viscosity of supercritical CO₂ (SC-CO₂) is 1 or 2 orders of magnitude smaller than that of normal liquid water, and it is still lower than that of liquid CO₂ (L-CO₂) formed in the lower temperature. Although the features of cracks induced by hydraulic fracturing (HF) with a low-viscosity fluid are expected to be different from those induced by conventional HF using water, the difference has been examined by only visual inspection [Kizaki *et al.*, 2013] and numerical simulations [Zhou and Burbey, 2014]. Thus, we conducted HF experiments varying viscosity of fracturing fluid in 170 mm cubic granite blocks with AE (acoustic emission) monitoring, to investigate how fluid viscosity affects the HF process and crack properties.

Early experiments of HF using rectangular blocks in under true triaxial stress are found in Haimson and Fairhurst [1969] and Cheung and Haimson [1989]. They used 125 × 125 × 140 mm blocks of hydrostones and similar size Niagara dolomite to examine validity of breakdown pressure and shut-in pressure for HF

Table 1. Specimen Number, Fracturing Fluid, and *P* Wave Velocity

Specimen No.	Fracturing Fluid	<i>P</i> Wave Velocity (km/s)		
		V_X	V_Y	V_Z
G1115	SC-CO ₂	4.25	4.86	4.72
G1202	SC-CO ₂	5.16	5.68	5.67
G1213	L-CO ₂	4.88	5.32	5.26
G1209	L-CO ₂	4.75	5.40	5.33
G1102	Water	4.05	4.86	4.72
G1103	Water	4.25	5.00	4.72
G1114	Oil	4.05	4.72	4.60
G1112	Oil	4.25	4.86	4.60
Average		4.46	5.09	4.95

stress measurement. Guo et al. used 305 × 305 × 305 mm and 610 × 584 × 305 mm gypsum blocks to examine the effect of specimen size on breakdown pressure [Guo et al., 1993a], leak-off phenomena [Guo et al., 1993b], and communication of two wells [Guo et al., 1993c]. Following their works, Morita et al. [1996] investigated the sealing effect of the drilling mud on stabilization for a borehole in HF experiments using

762 × 762 × 762 mm blocks of Berea sandstone, Castlegate sandstone, and Mancos shale. More recently, Bunker and Detournay [2008] made HF experiments in transparent polymethyl methacrylate and borosilicate glass blocks measuring 200 × 200 × 150 mm to investigate crack extension behavior driven by injected fluid. We also conducted HF experiments injecting water and viscous oil into 190 × 190 × 190 mm granite blocks under biaxial stress [Ishida et al., 2004] and SC-CO₂ and L-CO₂ into 170 × 170 × 170 mm granite blocks under hydrostatic stress to investigate effect of fracturing fluid viscosity on feature of cracks [Ishida et al., 2012]. Following these preliminary experiments, in this paper, we show the results of HF experiments injecting SC-CO₂, L-CO₂, water and viscous oil, the viscosities of which ranged from 0.051 to 336.6 mPa·s, into 170 × 170 × 170 mm granite blocks under the identical true triaxial stress condition, focusing on the AE source distribution, the AE mechanism, and the microstructure of the cracks revealed by using an acrylic resin containing a fluorescent compound imbibed to the material after the experiment. The results consistently showed the tendency that a low-viscosity fluid, such as SC-CO₂, induces more three-dimensionally sinuous cracks with more secondary branches than a higher viscosity fluids such as water and viscous oil.

2. Experimental Method

2.1. Specimens and Experimental Setup

We used eight cubes (170 × 170 × 170 mm) of granite with a 20 mm diameter central hole. The granite is produced in Kurokami-jima Island in Seto Inland Sea in Southwestern Japan. The material is commonly known as Kurokami-jima granite. The modal composition of the samples for our experiments was about 40% potassium feldspar, 36% plagioclase, 21% quartz, and 3% micas and accessories. The mean grain size was about 2 mm, and some coarse potassium feldspar grains whose size more than 5 mm were observed.

To confirm the reproducibility of the experimental results, we used two specimens for each of the fracturing fluids: SC-CO₂, L-CO₂, water, and viscous oil (Table 1). The inherent rift plane of the granite specimen was oriented to correspond to the YZ plane in the Cartesian coordinate system (Figure 1). As shown in Table 1, the average *P* wave velocities measured along the Y and Z directions were around 5.0 km/s, whereas that along the X direction normal to the rift plane was around 4.5 km/s. The *P* wave velocities were measured before the experiments without any confining pressure. Results of Brazilian tests with the discs oriented to make fracture along the rift plane on 33 cylindrical samples of the same kind of Kurokami-jima granite, measuring 45 mm diameter and 30 mm length, showed an average tensile strength of 3.38 MPa with a standard deviation of 0.21 MPa [Ishida et al., 2005]. Effective porosity of the granite was 0.84%, where the pore and the bulk volumes were measured with the saturation and the buoyancy methods, respectively [International Society for Rock Mechanics, 1979], and its intrinsic permeability obtained by air permeability test for hollow cylinder samples was around $9 \times 10^{-19} \text{ m}^2$ [Ishida et al., 2006]. The intrinsic permeability corresponds to $1 \times 10^{-11} \text{ m/s}$ of hydraulic conductivity, which is within the extent from 10^{-12} to 10^{-8} m/s for general granitic rock shown by Vutukuri and Katsuyama [1994]. To monitor AE events induced by the fluid injection, we glued four cylindrical lead zirconate titanate (PZT) elements 4 mm in diameter and 4 mm thick on each of the four lateral surfaces (total of 16 elements) of the specimen (Figure 1). To apply confining pressures, we covered each lateral surface with a 6 mm thick hard nylon sheet with four 5 mm diameter holes in the positions of the PZT elements. The PZT element wires were guided

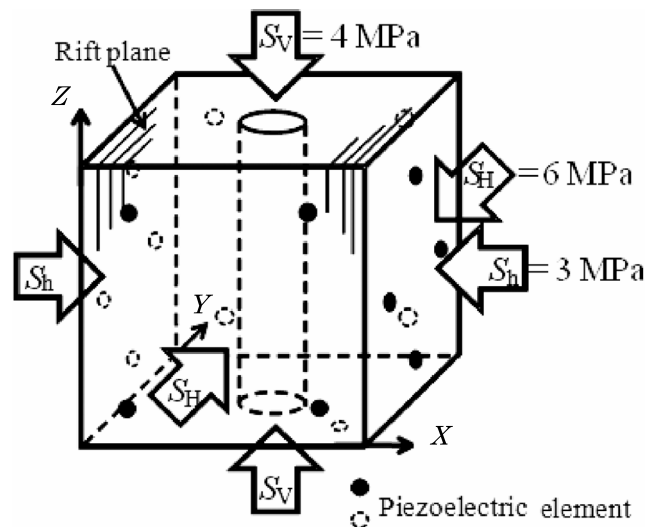


Figure 1. Coordinate system and loading condition of the specimen. The filled circles indicate the piezoelectric elements used as AE sensors at open positions, while the open circles with broken lines indicate those at hidden positions behind the specimen.

through grooves in the surface of the sheet, and the sheet was covered again with another 4 mm thick hard nylon sheet.

We placed the specimen in dry condition in a cylindrical pressure cell, except only the case of SC-CO₂ injection where we filled the cell with hot water to prevent the injected CO₂ from cooling. We inserted four bow-shaped spacer blocks between the specimen and the inner wall of the pressure cell and placed a flat jack between the specimen and each spacer block to apply pressure in the X and Y directions (Figure 2). In the Z direction, we placed flat jacks between the specimen and loading plates supported by the end caps on the top and bottom of the pressure cell. In all experiments, we applied confining pressures of 3, 6, and 4 MPa in the X, Y, and Z directions, respectively, to provide the deviatoric stress. The stress magnitudes of 3 and 6 MPa were selected following the solution by Kirsch [1898] so as to keep compressive stress larger than 3 MPa in the tangential direction all along the hole wall. The minimum tangential stress of 3 MPa induced at the points of the Y direction along the hole wall did not exceed the capacity of the injection pump and pipe line to induce HF, and the maximum stress of 15 MPa induced at those of the X direction was sufficiently smaller than that inducing the borehole breakout. The stress magnitude of 4 MPa in the Z direction was selected so as to be between 3 and 6 MPa in the X and Y directions. Although the confining pressures increase P wave velocities, we ignored the increases in calculation of AE source location, because they were expected only

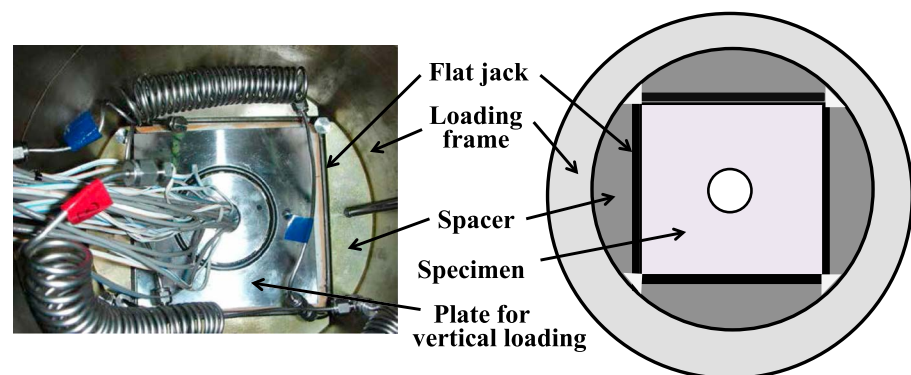


Figure 2. (left) Photo and (right) cross-sectional schematic of a specimen, flat jacks, and spacers set in the loading frame. In the photo, the specimen is set under the plate for the vertical loading.

around 0.1 to 0.3 km/s from the measurements for granite under confining pressure from 0 to 200 MPa [Sano *et al.*, 1992].

2.2. Method of Fluid Injection

Figure 3 shows the packer inserted into the central hole of the samples to inject the fracturing fluids, including CO₂. The packer had a 60 mm pressurizing section sealed with two O-rings at each end. The pressurizing section was centered along the hole. In all the experiments, we injected the fracturing fluid under the control of syringe pump to keep the same constant flow rate of 10 mL/min and stopped the injection just after HF was induced, which was indicated by a sudden pressure drop.

Figure 4 shows the injection system used for the HF experiments. To make SC-CO₂, we fed CO₂ from a bomb to a syringe pump cylinder, which had a capacity of 266 mL. To fill the cylinder as full as possible, we cooled the CO₂ to keep it in the liquid state by circulating coolant in a cooling unit above the cylinder. The phase diagram in Figure 5 shows that CO₂ becomes supercritical when the temperature is higher than 31.0°C and the pressure is greater than 7.38 MPa. After discharging L-CO₂ from the cylinder of the syringe pump at a constant flow rate of 10 mL/min, we heated it with a heater unit. We maintained the temperature at 55°C by bandaging electric resistance heating ribbon along the pipe connecting the heater unit to the packer (Figure 4). In addition, we filled the cell containing the specimen with hot water at a temperature of around 45°C to prevent the injected CO₂ from cooling. Although we did not measure the thermal properties of the Kurokami-jima granite, we believe that the temperature in the specimen did not easily increase within 1 h or so for the SC-CO₂ experiment, even when the outside of the specimen was warmed with the hot water and the wall of the injection hole wall with SC-CO₂. This expectation comes from our experiences in the heater test in a block of Inada granite whose thermal conductivity is 3.3 W/(m K), specific heat is 0.72 J/(g K), and density is 2.0×10^3 kg/m³ [Ishida *et al.*, 1990]. The similar tendency was also found in heater test in a block of Lac du Bonnet granite by Jansen *et al.* [1993]. Thus, during the experiment, it is most likely that the temperature of the specimen only in the vicinity of the surfaces and the hole wall was kept around 40°C, while the temperature in the specimen was kept at the room temperature around 20°C in which the specimen was left more than 1 week before the experiments. Although the specimen was soaked in hot water for around 1 h, the water was not expected to infiltrate around the injection hole owing to the specimen's low permeability, and the HF was induced under almost dry conditions based on our experience from similar previous experiments. For the other fluids, including L-CO₂, HF was also induced under dry conditions at room temperature, because we fed the fluids to the packer without heating or filling the cell with water.

2.3. Methods for Monitoring AE, Pressure, and Temperature

The PZT elements glued onto the specimen had a resonance frequency of 300 kHz, and they were covered with an aluminum sheet to avoid electromagnetically induced noise. They were also covered with heat shrinkable tubes and silicone rubber to provide a waterproof barrier for SC-CO₂ fracturing. We amplified the AE signals by 72 to 84 dB in total (36 dB in a preamplifier and 36 to 48 dB in a signal conditioner), processed them with a band-pass filter between 80 kHz and 1 MHz, and recorded them on a hard disk through an analog-to-digital (A/D) converter (PXI-5105, National Instruments Corp.) under the control of LabVIEW program. Since the A/D converter has 16 separate channels, the processed AE signals were digitized with 0.1 μ s sampling time and had 2048 samples in the record length for each event for each sensor. We set the dead time after recording an event to 1 ms to prevent the hard disk from recording too much noise caused by "ringing," which is the vibration following a large AE event. The recording of an AE event was triggered when one of the signals from the 16 AE sensors exceeded 3 V. In addition, we counted the number of AE events per second for each AE sensor when the signal exceeded 3 V.

Every 0.1 s, we measured the injected fluid pressure through transducers (PW-50MPa, Tokyo Sokki Kenkyujo Co., Ltd., with a full scale of 50 MPa and precision of 0.1 MPa) at the top of the packer, and the flat jack pressures in the X, Y, and Z directions through transducers (PW-20MPa with a full scale of 20 MPa and precision of 0.04 MPa) on the connecting pipes of opposing pairs of flat jacks. We measured the temperature changes with T-type thermocouples, which can measure temperature from -200 to 400°C with resolution of 0.5°C , glued to the injection pipe just above the packer in the hole and at both ends of the section of pipe covered with electric resistance heating ribbon only for SC-CO₂ injection (Figure 4).

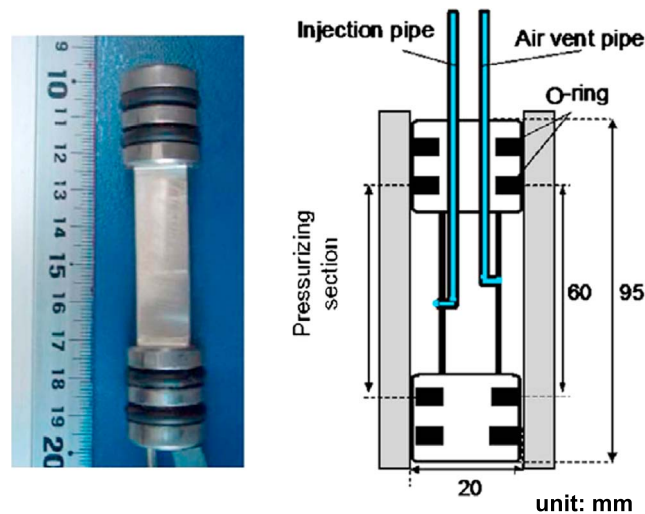


Figure 3. Straddle packer used to inject fracturing fluid including CO₂. (left) Photo and (right) cross-sectional schematic of the packer.

2.4. Observation of Cracks With Fluorescent Resin

After the HF experiment, we overcored the tested specimens with a diameter of 68 mm along the central injection hole (Figure 6). The overcored hollow cores were soaked in the thermosetting acrylic resin monomer containing a fluorescent compound under vacuum to allow the resin monomer to penetrate into the induced cracks and then heated to set the resin in the cores before sectioning. The cracks filled with the resin were visualized and observed under the ultraviolet light irradiation [Nishiyama and Kusuda, 1994]. We made two thin sections including hydraulically induced fractures on the plane where $Z = 85$ mm, corresponding to the center of the pressuring section. No secondary fractures caused by preparing the thin sections were detected because the above mentioned pretreatment was completed before sectioning.

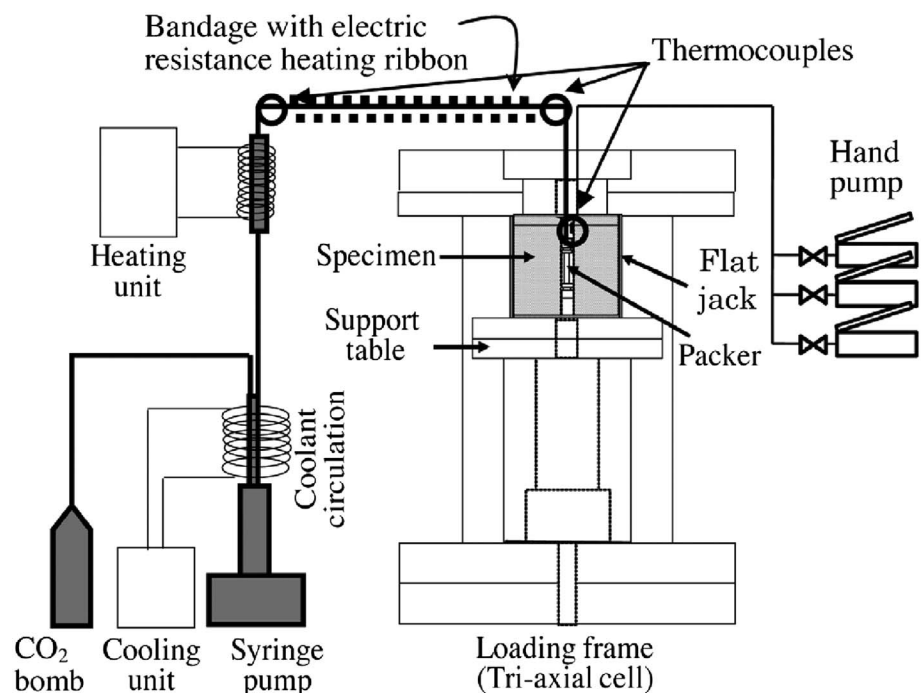


Figure 4. Schematic of system for injecting fracturing fluid and loading confining pressure.

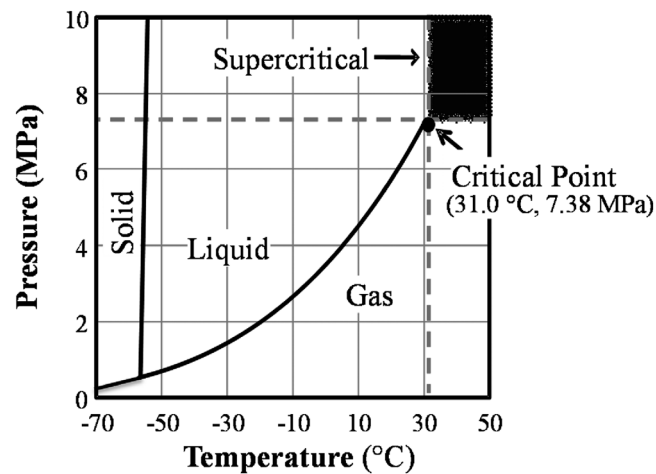


Figure 5. Phase diagram of CO₂.

3. Results

Table 2 summarizes our experiments. Because both specimens for each fluid showed similar trends, the results for only one specimen per fracturing fluid are shown. These specimens are G1115 for SC-CO₂, G1213 for L-CO₂, G1102 for water, and G1114 for viscous oil (open circles in Table 2).

3.1. Changes in Fluid Pressure and AE Count Rate

Figure 7 shows the changes in injected fluid pressure, confining pressure, and AE count rate during injection of SC-CO₂, L-CO₂, water, and viscous oil into the specimen. The temperature is shown only for SC-CO₂. In the injection of SC-CO₂ and L-CO₂, since we fed CO₂ from the bomb, the bomb pressure around 5 MPa applied in the hole just after the experiments have started. In contrast, in the injection of water and oil, the pressure increased gradually from zero. In all cases, we shut the return pipe after filling the fluids in the dry empty pressurizing section in the hole, and we kept to inject the fluids at the constant flow rate of 10 mL/min through the experiments. The elapsed time along the lateral axis is taken as zero when the breakdown pressure, which is defined as the peak pressure just before large sudden pressure drop, is recorded.

In Figure 7a for the case of SC-CO₂ injection, we show the temperature measured with a thermocouple glued on the injection pipe just above the packer in the hole. The temperature most likely indicates the CO₂ temperature, since the temperature always showed the same temperature measured at the both ends of the section of pipe covered with electric resistance heating ribbon (see Figure 4) even when the sudden temperature change of the CO₂ was induced. Since the temperature shows around 36°C, the test began with the CO₂ in the gas state in the borehole, referring to the phase diagram of CO₂ shown in Figure 5. The CO₂

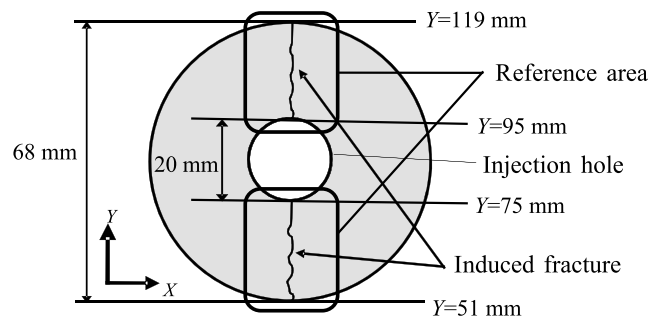


Figure 6. Overcored hollow core for microscopic observation and reference areas on a thin section.

Table 2. Summary of Experiments

Specimen No.	Fracturing Fluid	Date of Experiment	Temperature (°C)	Viscosity (mPa s)	Breakdown Pressure, P_b (MPa)	Tensile Strength, T (MPa) ^a	No. of AE Sources	L_{av} (mm)	Fractal Dimension	Ratio of Compression (%)	Tortuosity L/L_0	Av. no. of Branches
○ G1115	SC-CO ₂	12 Oct 2012	35.5	0.051	9.10	6.10	118	12.06	2.42	51.30	1.109	2,131
○ G1202	SC-CO ₂	11 Oct 2012	38.4	0.053	10.16	7.16	218	11.44	2.40	62.70	1.075	2,083
○ G1213	L-CO ₂	10 Dec 2013	12.8	0.097	11.96	8.96	160	10.78	2.17	54.21	1.120	1,870
○ G1209	L-CO ₂	16 Jan 2014	6.0	0.108	11.98	8.98	81	12.52	2.15	54.80	1.102	1,927
○ G1102	Water	14 Sep 2011	31.4	0.774	12.96	9.96	116	8.15	2.20	56.67	1.095	1,789
○ G1103	Water	15 Sep 2011	30.5	0.788	13.33	10.33	72	9.35	2.42	61.42	—	—
○ G1114	Oil	1 Dec 2011	11.1	316.0	23.07	20.07	73	7.39	2.01	69.01	1.062	1,704
○ G1112	Oil	2 Dec 2011	10.6	336.6	25.05	22.05	62	8.51	1.96	72.11	1.054	2,029

^aTensile strength is obtained from the equation (3), $T = (1 + \alpha)P_b - 3$, when $\alpha = 0$. (A unit for T and P_b is MPa and α is a coefficient having no dimension.)

should start to become into a supercritical state once the fluid pressure get closer to around the critical pressure, 7.38 MPa. This change could be inferred from the change in the increase rate of the fluid pressure under the constant flow rate as shown with the arrow in Figure 7a. This change was most likely caused by the decrease of the fluid compressibility due to the change from the gas to the supercritical state of CO₂. The fluid pressure decreased sharply to zero just after breakdown at 9.10 MPa. The pressure and temperature, 35.5°C, at the breakdown demonstrate that the HF was induced by CO₂ of a supercritical state. The pressure decrease, which was caused by leakage through fracturing-induced cracks, most likely changed the CO₂ from supercritical to gas state again. The temperature also decreased to 22.6°C just after breakdown, and came back to 27.9°C at 100 s after the breakdown. The temperature decrease was probably caused by adiabatic expansion of CO₂, because the measured temperature decrease from 35.2 to 22.6°C can be induced by 1.15 times larger expansion of the sealed volume of gas state CO₂, under an assumption of simple adiabatic expansion using Poisson's law. The AE count rate (average of the 16 AE sensors) increased sharply just after breakdown and events continued to occur for several tens of seconds. The confining pressures, S_H , S_V , and S_h (Figure 1), were kept nearly constant at 6, 4, and 3 MPa, respectively, with small fluctuations due to crack growth during breakdown.

Breakdown pressure was positively correlated with viscosity: 9.10 MPa for SC-CO₂, 11.96 MPa for L-CO₂, 12.96 MPa for water, and 23.07 MPa for viscous oil.

3.2. AE Source Locations

Figure 8 shows the locations of AE sources observed during the fluid injections projected onto the three orthogonal planes (XY, YZ, and ZX). All of the AE occurred within 15 s after breakdown. Waveforms of a typical AE event for the respective four fluids are shown in Figure S3 in the supporting information.

As a source location method, we used the iterative method with the least squares principle, which is called Geiger's method [Geiger, 1910, 1912] following the classification by Ge [2003a, 2003b]. Considering the anisotropy of the P wave velocity [Rothman *et al.*, 1974], which was measured before the experiment shown in Table 1, the AE source locations were determined within an expected accuracy of several millimeters. This was possible because we chose the AE events satisfying the following criteria [Ishida and Sasaki, 2011]: (i) five or more P wave arrival times could be read and (ii) the standard deviation and the maximum of residuals of arrival times were within 3 μ s. The number of sources that satisfied these conditions was 118 for SC-CO₂ (Figure 8a), 160 for L-CO₂ (Figure 8b), 116 for water (Figure 8c), and 73 for viscous oil (Figure 8d). Figure 8 also shows the cracks visible on the original surfaces of the cubic specimens with the located sources. Cracks were visible on the two opposite surfaces of the XY plane for SC-CO₂ (Figure 8a), the XY and ZX planes for L-CO₂ (Figure 8b), and

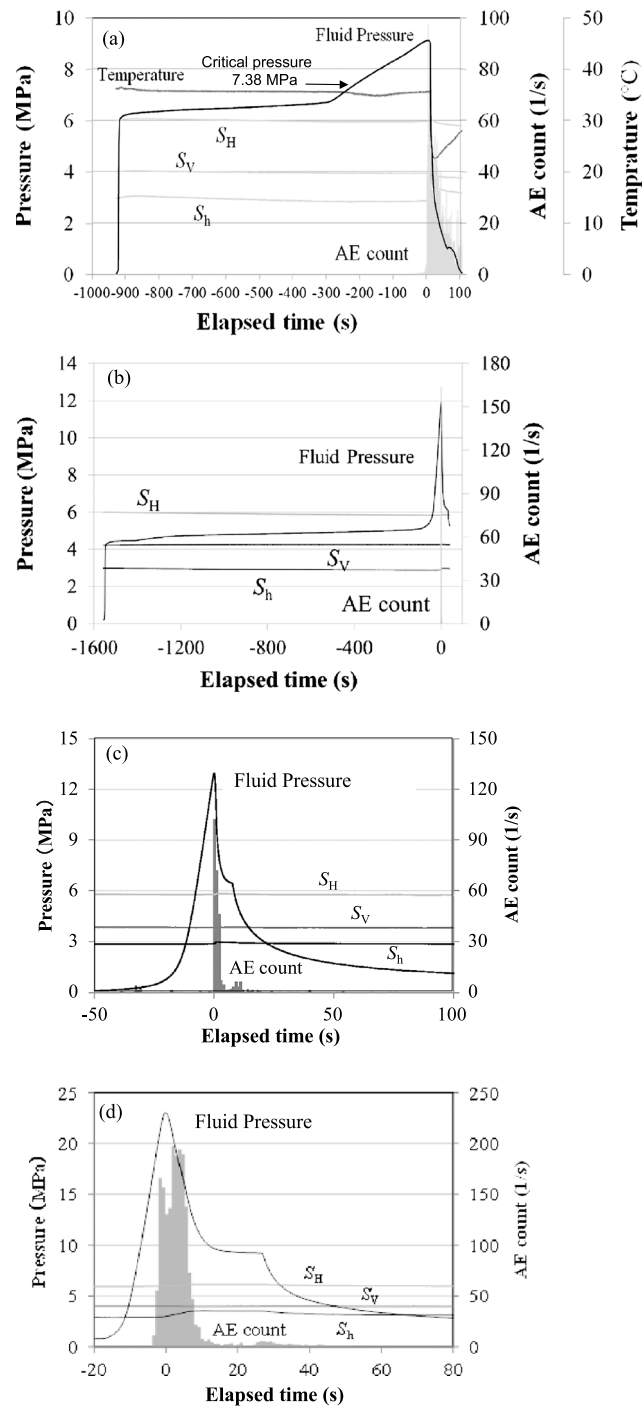


Figure 7. Changes in injected fluid pressure, confining pressure, and AE count rate for (a) SC-CO₂, (b) L-CO₂, (c) water, and (d) viscous oil. The temperature change is only shown in Figure 7a. The scales of the vertical and horizontal axes differ between plots.

the ZX plane for viscous oil (Figure 8d). The cracks contained in the two parallel planes are distinguished by using dark lines (near planes; $Z = 170$ mm for the XY and $Y = 0$ mm for the XZ planes) and light lines (far planes; $Z = 0$ mm for the XY and $Y = 170$ mm for the XZ planes). The other cracks were visible on one plane only, while no visible crack appeared on the YZ planes.

The AE sources were distributed along the cracks, as expected from the observed surface cracks. However, the AE sources in Figure 8a were more widely distributed rather than lying along a flat plane; this effect seemed to

increase with the decrease of viscosity of the fracturing fluids. To present the differences quantitatively, the maximum likelihood flat plane for the AE distribution was first estimated for each specimen by minimizing the sum of squares of the distances from a source to the flat plane. After that, the average distance, L_{av} , from a source to the maximum likelihood plane was obtained. For the AE distributions shown in Figure 8, the L_{av} values were 12.06 mm for SC-CO₂, 10.78 mm for L-CO₂, 8.15 mm for water, and 7.39 mm for viscous oil.

We obtained also the fractal dimensions of the AE distributions with the correlation function method, following Hirata *et al.* [1987] and Grassberger [1983]. Theoretically, the fractal dimensions of an infinite number of points distributed on a line, on a plane, and in three-dimensional space are 1, 2, and 3, respectively. However, because the number of distributed points is finite, the fractal dimensions obtained by this method tend to be slightly lower than their respective dimensions [Ishida *et al.*, 1998]. Nevertheless, fractal dimension is useful for characterizing the features of the AE distribution, and a larger fractal dimension suggests more extensive cracking in three dimensions. For the AE distributions shown in Figure 8, the fractal dimensions for SC-CO₂, L-CO₂, water, and viscous oil were 2.42, 2.17, 2.20, and 2.01, respectively. This suggests that a low-viscosity fracturing fluid such as SC-CO₂ induces cracking in three dimensions rather than in two by, for example, forming sinuous cracks with a greater number of secondary branches.

3.3. Induced Crack Patterns Observed With the Fluorescent Method

The cracks induced by HF in the experiments were subtle in the all cases, and they were barely identified by tracing segments where the fracturing fluid leaked on the surfaces of the cubic specimens, although they seemed to be observed the more clearly the more viscous the fracturing fluid became. Even when we overcored with a 68 mm diameter around the 20 mm diameter injection hole, the overcored hollow core still had substantial strength and did not break into two pieces for almost all of the cases, as seen in the experiments by Schmitt and Zoback [1992, 1993].

Figure 9 shows crack propagation patterns observed on the thin sections cut from the hollow cores soaked in the acrylic resin containing a fluorescent compound. Although preliminary observations, except for the L-CO₂ injection, have already been reported [Chen *et al.*, 2015], we examine the crack patterns in relation to the results of AE monitoring. Figures 9a(i) and 9b(i), 9b(ii), 9c(i), and 9d(i) show fluorescent images of the thin section taken under ultraviolet light [Nishiyama and Kusuda, 1994]. The bright and bluish white regions correspond to cracks. Figures 9a(ii), 9b(iii), 9c(ii), and 9d(ii) show sketches of the main crack induced by the injection. The crack propagates from right to left in all figures. The periphery of the injection hole is shown with a red line on the right side of the sketch. The observed area corresponds to the area from Y coordinate of 95 to 119 mm in Figure 6, and the left side almost corresponds to the inner wall of the overcoring hole. The sketch was made by connecting segments of the main crack identified with the fluorescence method under ultraviolet light, considering the continuity in the direction of the crack propagation. Although it was easy to identify the main cracks in the photos of SC-CO₂, water, and viscous oil (Figures 9a(i), 9c(i), and 9d(i)), it is difficult only in the photo of L-CO₂ (Figure 9b(i)); therefore, we used an enlarged photo (Figure 9b(ii)). The sketches of the main cracks in Figures 9a(ii), 9b(iii), 9c(ii), and 9d(ii) show that the cracks are tortuous and never propagate straight, although they propagate along the direction of the maximum compressive stress and along the rift plane where the main preexisting microcracks align. Fluids with lower viscosity induce cracks with higher tortuosity, because intermittent and stepwise crack extensions become more conspicuous.

To examine the correlations between crack patterns and the constituent mineral grains of the specimens, photomicrographs of the crack patterns on thin sections for SC-CO₂ and oil injection in the boxes in Figure 9 were taken using a petrographic microscope in crossed-polarized light (crossed Nicols). The cracks induced by SC-CO₂ propagate mainly along the grain boundaries of the constituent minerals (Figure 10a). In contrast, Figure 10b shows that the cracks induced by oil cut through many mineral grains. This is most likely a reason why the crack pattern depends on the viscosity of the fracturing fluid.

Crack aperture shown in Figure 10a is larger than that in Figure 10b, although Ishida *et al.* [2004] and Stanchits *et al.* [2014] showed that the higher viscosity fracturing fluid tends to induce cracks having larger aperture. Ishida *et al.* [2004] injected water and viscous oil into blocks of Kurokami-jima granite with monitoring pressure change of the flat jacks applying the confining pressure. Stanchits *et al.* [2014] injected two kinds of silicon oil having thousandfold different viscosity into low permeability blocks of

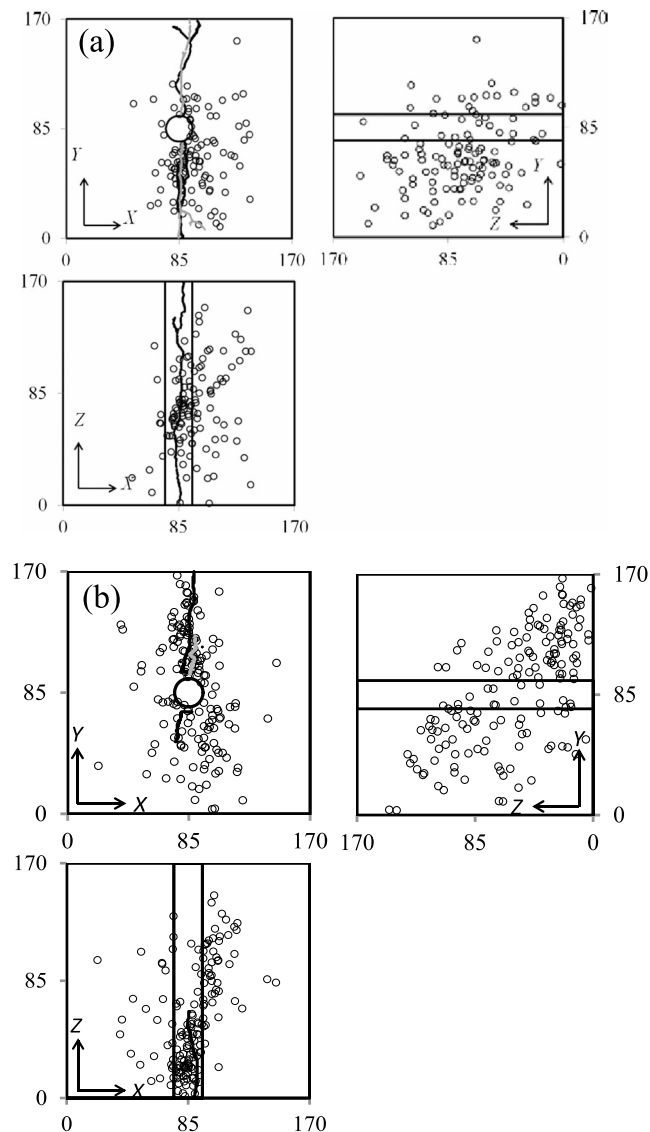


Figure 8. AE source distribution and cracks visible on the specimen surface for (a) SC-CO₂, (b) L-CO₂, (c) water, and (d) viscous oil. Dark and light lines show cracks that appeared in different planes facing each other.

Colton sandstone with monitoring volume of the injected fluid. Their results both indicated that the higher viscosity tends to induce the larger aperture cracks, which is inconsistent with our results shown in Figure 10. Although we did not monitor changes of the flat jack pressure and the injected volume, the large aperture observed in the SC-CO₂ injection was probably caused by expansion of CO₂ with the phase change from SC-CO₂ to gas due to the pressure decrease after the crack extension to the lateral free surface of the specimen.

4. Effect of Fluid Viscosity

In Figure 11, we show the dependency on the fracturing fluid viscosity of breakdown pressure, the AE distribution, and fracturing mechanism based on ratios of the *P* wave first motion polarity of AE events and the crack features observed by the fluorescence method. To confirm the generality of the properties, we show data for our chosen specimens described in the previous section and for the alternate specimens G1202 for SC-CO₂, G1209 for L-CO₂, G1103 for water, and G1112 for viscous oil (Table 2). The viscosities of SC-CO₂

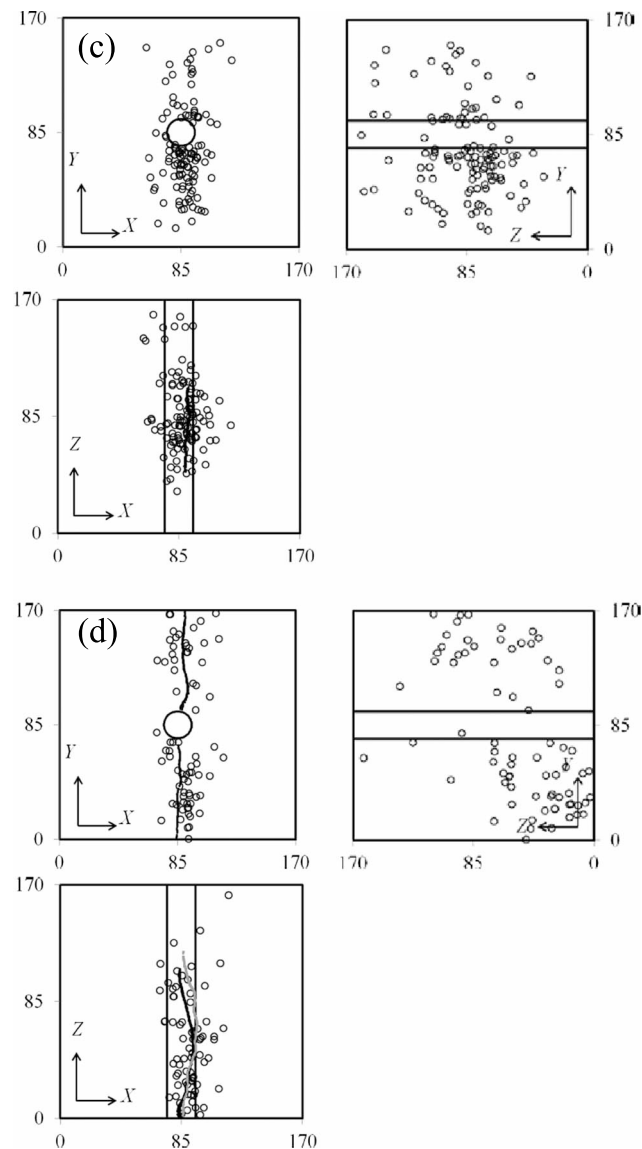


Figure 8. (continued)

and L-CO₂ in Figure 11 were estimated from the temperature and pressure at breakdown, following the equation of state for CO₂ implemented by *Ohmori* (<http://hp.vector.co.jp/authors/VA030090/>) based on the theory by *Fenghour et al.* [1998]. The viscosities of the water were obtained from Chronological Scientific Tables [National Astronomical Observatory of Japan, 1995], and those of the oil were obtained from a table provided by the oil manufacturer, by using the temperatures measured during the experiments.

4.1. Breakdown Pressure and Apparent Tensile Strength

Figure 11a shows the dependency of breakdown pressure on fracturing fluid viscosity. This figure clearly shows that breakdown pressure increases with viscosity. The tendency is consistent with the experimental results by *Morita et al.* [1996] using water-based and oil-based muds and, in addition, the numerical simulation by *Bunger et al.* [2010].

Schmitt and Zoback [1992, 1993] discussed carefully the effect of pore pressure on crack initiation of HF through laboratory experiments using hollow cylinder of westerly granite and glass, where they changed the pressurization rate and the magnitude of the confining pressure applying the outer surface of the

cylinder. Here we discuss the effect in the much simpler way than *Schmitt and Zoback* [1992, 1993], using the following equation proposed by *Scheidegger* [1962] for a vertical borehole:

$$P_b = 3S_{h\min} - S_{H\max} + T - P_p \quad (1)$$

where P_b the breakdown pressure, P_p the pore pressure, T the tensile strength, $S_{h\min}$ the minimum horizontal stress, and $S_{H\max}$ the maximum horizontal stress. In our experiments, $S_{h\min}$ and $S_{H\max}$ correspond to S_h and S_H , respectively, as shown in Figure 1. By putting that $S_{h\min} = S_h$, $S_{H\max} = S_H$ and $P_p = \alpha P_b$, the equation (1) becomes

$$T = S_H - 3S_h + (1 + \alpha)P_b. \quad (2)$$

The case that $\alpha = 0$ corresponds to the state that no pore pressure applies without infiltration of fracturing fluid, while the case that $\alpha = 1$ corresponds to the state that the pore pressure equal to the fracturing fluid pressure applying on the wall of the injection hole. The magnitude of S_h fluctuated at the breakdown, because a specimen expanded in the X direction, due to intrusion of fracturing fluid into a crack induced along the Y direction, and resulted to push the flat jacks applying the confining pressure, S_h . However, since the fluctuation is not so large as shown in Figure 7, by substituting 3 MPa for S_h and 6 MPa for S_H , the equation (2) becomes

$$T = (1 + \alpha)P_b - 3. \quad (3)$$

where a unit for T and P_b is MPa and α is a coefficient having no dimension.

The apparent tensile strength, T , obtained from the equation (3) is shown in Table 2 for the cases that $\alpha = 0$. Even in the case that $\alpha = 0$, the apparent tensile strength, T , becomes from 6 to 22 MPa, which is much larger than Brazilian tensile strength of the Kurokami-jima granite, 3.38 MPa. In the case that $\alpha = 1$, the apparent tensile strength, T , becomes still much larger.

In Brazilian test, the tensile stress uniformly distributes along the fracture plane, while in our HF experiment, the tensile stress in the circumference direction is the largest on the wall of the injection hole and decreases with the square of the distance from the center of the hole [*Kirsch*, 1898]. When the difference of the stress distribution is taken account by introducing a concept of "risk of rupture" proposed by *Weibull* [1939a, 1939b] under the assumption of uniform distribution of Griffith cracks, the breakdown pressure, P_b , becomes 1.45 times larger than that of the Brazilian tensile strength [*Ishida et al.*, 2005]. The difference of 1.45 times showed good agreement with that of 1.47 obtained in their experiments [*Ishida et al.*, 2005]. However, the difference is still small to explain the difference between the apparent tensile strength and the Brazilian tensile strength.

The cracks induced in our HF experiments seemed to extend instantaneously to the lateral surface of the specimen. Discussion on the crack extension considering the stress intensity factors at a crack tip, as described by *Ishida et al.* [1997] following *Zoback et al.* [1977] and *Zoback and Pollard* [1978], may help to interpret the difference in the apparent tensile strength depending on the viscosity of the fracturing fluid. Figure 12 (left column) depicts the case in which hydrostatic pressure, σ , applies throughout an ellipsoidal crack surface. In this case, $K_I = \sigma(\pi l)^{1/2}$, where K_I is the stress intensity factor of mode I at a crack tip and l is half of the crack length. According to this relation, the stress intensity factor at a crack tip increases with crack length; in other words, a crack never stops once it starts to extend. Figure 12 (right column) depicts the case in which a pair of point loads, F , are applied at the center of an ellipsoidal crack. In this case, $K_I = F(\pi l)^{-1/2}$, which indicates that stress intensity factor at a crack tip decreases with crack length; that is, a crack never extends without an additional increase in applied loads. It can be expected that the fracturing fluid pressure reaches the closer to a crack tip, the lower the viscosity becomes. Thus, the low-viscosity fluid injection would make state close to that hydrostatic pressure, σ , applies throughout an ellipsoidal crack surface, while the high-viscosity fracturing fluid injection would make state close to that a pair of point loads, F , applies at the center of an ellipsoidal crack. Consequently, the difference of the apparent tensile strength, T , in other words, the difference of the breakdown pressure, P_b , among the fracturing fluids, is most likely caused by the differences of their viscosity. From the above discussion, in field operations for the same rock type stratum under the same in situ stress condition and flow rate, the breakdown pressure for injecting a low-viscosity fluid, such as SC-CO₂, is expected to be lower than that of water and much lower than that of high-viscosity fluid such as gel.

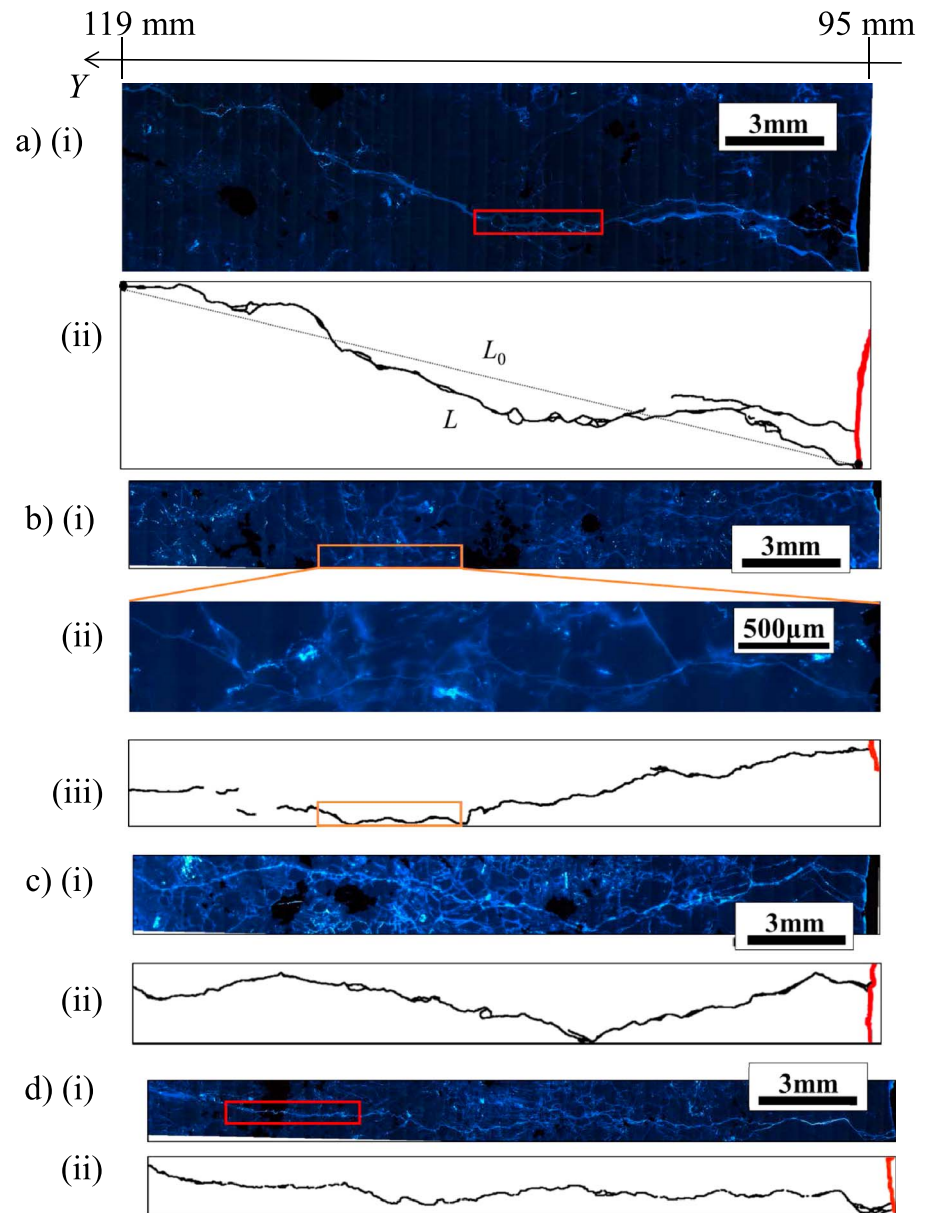


Figure 9. Fracture propagation patterns observed on thin sections using the fluorescent method from 95 to 119 mm in the Y coordinate in Figure 6. Specimens fractured by (a) SC-CO₂ [G1115], (b) L-CO₂ [G1213], (c) water [G1102], and (d) viscous oil [G1114]. Figures 9a(i) and 9b(i), 9b(ii), 9c(i), and 9d(i) show the photos taken of the thin section. Figures 9a(ii), 9b(iii), 9c(ii), and 9d(ii) show sketches of the main crack, and the red line on the right side indicates the periphery of the injection hole. In Figure 9b, an enlarged photo of area enclosed with the orange box is also shown to help identify the main crack. Cracks in the red boxes in Figures 9a and 9d are shown on the microphotos taken under polarized light in Figure 10. The symbols L_0 and L in Figure 9a show the lengths to calculate the tortuosity, L/L_0 , shown in Figure 11e.

4.2. AE Distribution

Figure 11b shows the dependency on viscosity of the average distance, L_{av} , from a source to the maximum likelihood plane. This figure clearly indicates that L_{av} decreases with viscosity. This suggests that low-viscosity fracturing fluids induce cracks that propagate farther away from a flat plane, whereas viscous fluids, such as gels, tend to induce cracks along a flat plane. Figure 11c shows that the fractal dimension, FD , of the AE distributions decreases with viscosity, suggesting that low-viscosity fracturing fluids induce cracks that propagate three dimensionally, rather than two dimensionally along a flat plane.

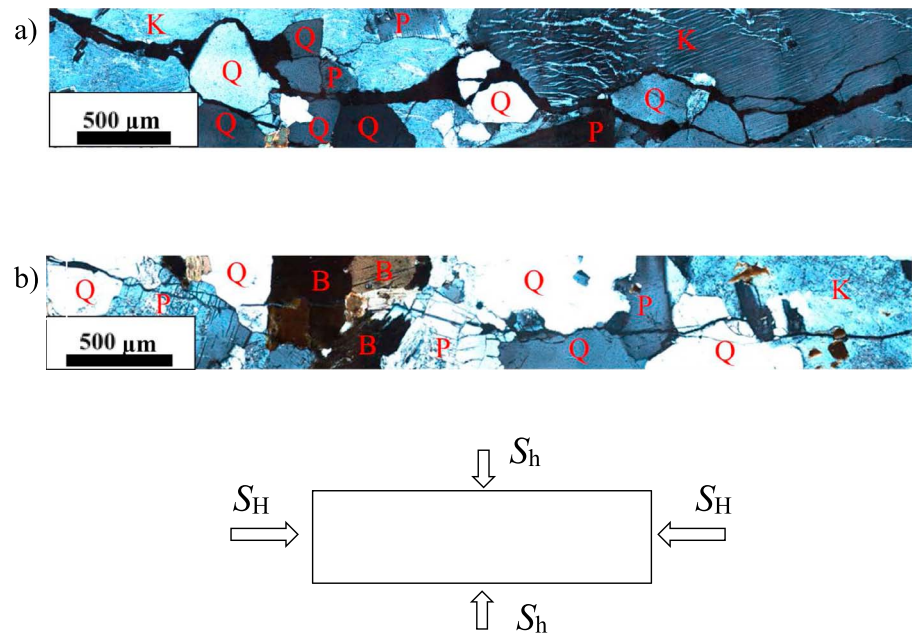


Figure 10. Observation on crack patterns and constituent mineral grains for (a) SC-CO₂ injection, red box in Figure 9a, and (b) oil injection, red box in Figure 9d, using a petrographic microscope in crossed-polarized light (crossed Nicols). (B: biotite, K: K-feldspar, P: plagioclase, and Q: quartz.) The bottom figure illustrates the stress condition when the cracks extended in the specimen.

4.3. Fracturing Mechanism Deduced From *P* Wave First Motion Polarity of AE

The differences in the crack features possibly arose from a difference in fracture mechanism. Thus, we compared ratios of the *P* wave first motion polarity of approximately 30 AE events that were detected by at least seven sensors, allowing *P* wave arrivals to be determined for a source location. A calibration test, in which a small steel ball was dropped onto the upper surface of a thick steel plate and the resultant waveforms were recorded by sensors glued onto the plate's lower surface, showed that compression corresponded to an upward trace and dilation to a downward trace. In Figure S3 in the supporting information, the closed triangles indicate compression in *P* wave first motion showing upward trace, while the open triangles indicate dilatation. For example, in the case of Figure S3a, since the number of compression is four and that of dilatation is four, the compression ratio in *P* wave first motion for this AE event becomes 50%. Figure 11d shows the compression ratio in *P* wave first motion tends to increase with viscosity. The ratio would be 50% for a pure shear fracture and 100% for a pure tensile fracture. Thus, the results suggest that a low-viscosity fracturing fluid tends to induce shear dominant fractures, whereas viscous fluids tend to induce tensile dominant fractures.

As shown in Figure 10a, the cracks induced by SC-CO₂ propagate mainly along the grain boundaries of the constituent minerals, producing many small cracks inclined in the direction of the maximum compressive stress, S_H , which is the propagating direction of a main crack. As shown in Figure 8, the induced main cracks extended in planes almost parallel to the *Z* direction (the direction of the intermediate principal stress, S_V) in the all experiments, and we observe the cracks on *XY* plane normal to the *Z* direction in Figure 10a. Thus, ignoring effect of the intermediate principal stress and considering the two-dimensional stress condition, because shear stress develops on a plane inclined in the direction of the maximum compressive stress, S_H , the inclined cracks are easy to be induced by shear fracture. In contrast, Figure 10b shows that the cracks induced by viscous oil injection cut through many mineral grains and propagate almost straight along the direction of the maximum compressive stress without bending. Because shear stress does not develop on a plane parallel to the direction of the maximum compressive stress, the cracks are probably induced by tensile fracture rather than by shear. In addition, in the oil injection, because the cracks extended to the both lateral surfaces of the specimens as shown in Figure 8d and the injected oil seeped out from the induced cracks on the specimen surfaces, the tensile cracks are most likely induced by the intrusion of the viscous oil.

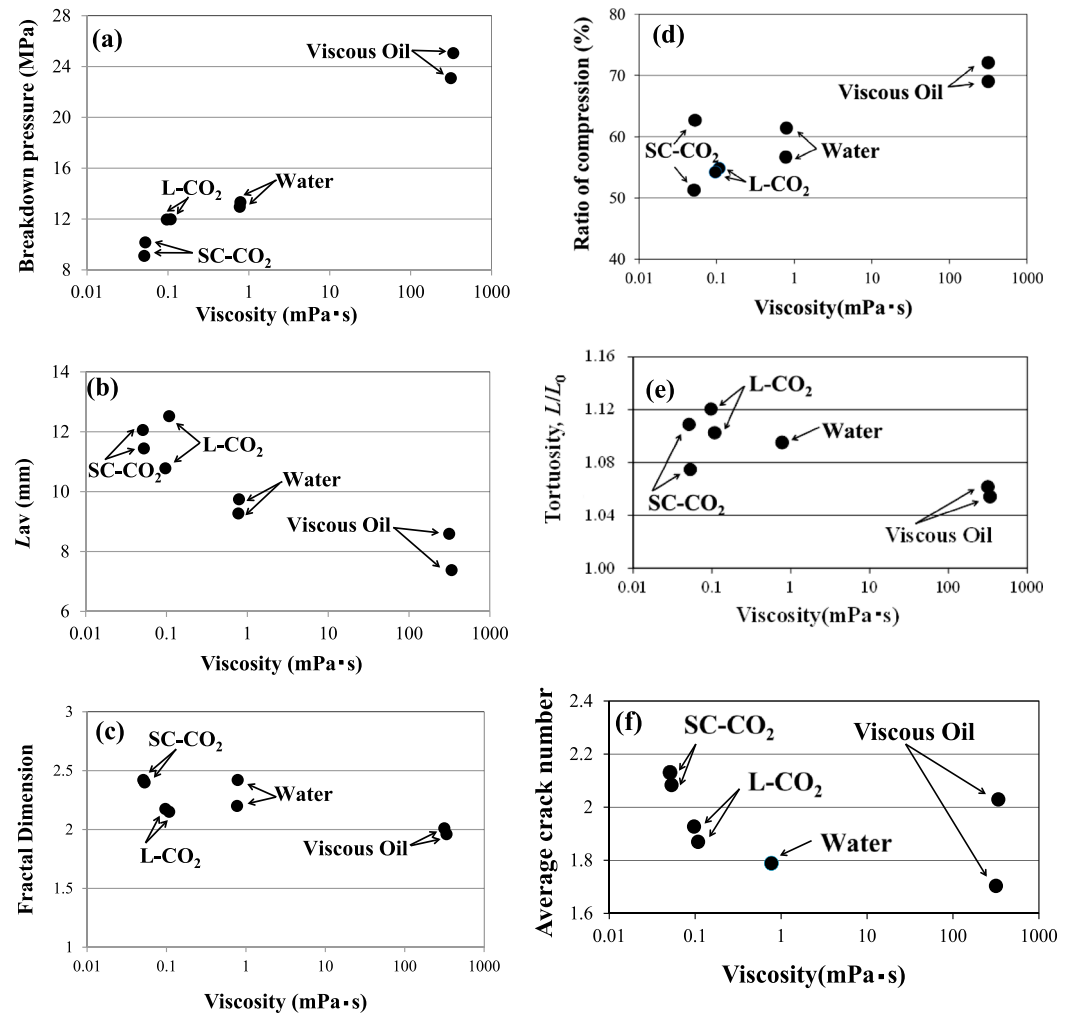


Figure 11. Effect of fracturing fluid viscosity on (a) breakdown pressure, (b) average distance L_{av} from a source to the estimated most likely plane, (c) fractal dimension, (d) the compression ratio to the total number of the polarities in P wave first motion, (e) crack tortuosity, and (f) average crack number. The results in Figures 11a–11d were derived from AE data, whereas the results in Figures 11e and 11f were from microscopic crack observation using the fluorescent method.

4.4. Crack Features Deduced From Direct Observation

Figure 11e shows the dependency on viscosity of the tortuosity, L/L_0 , where L is the crack length measured by connecting 0.05 mm long line segments, namely, a divider, along the main crack, and L_0 is the length of the straight line from the initiation point of the crack on the wall of the injection hole to its end point on the inner wall of the overcoring (Figure 9a). The main cracks are traced in both directions from the fracturing hole, from Y coordinates of 75 to 51 mm and from 95 to 119 mm (Figure 6). The tortuosity for each specimen is the average of the tortuosities obtained in the two opposite directions. Although the results for the two specimens for each fracturing fluid are plotted, only one result is plotted for the water injection. This is because the cracks in specimen G1103 for water injection could not be filled with the fluorescent resin, and no observation was obtained. The tortuosity of the induced cracks tended to increase with the decrease of fracturing fluid viscosity, which is consistent with the crack propagation patterns in Figure 9.

Figure 11f shows the dependency on viscosity of an average of the crack numbers, which were counted when the induced cracks crossed the scanning lines at intervals of 1 mm from the injection hole to the inner wall of the overcoring. We counted the cracks excluding preexisting cracks, voids, and other defects with checking the propagation direction and continuity of the cracks through careful observation of crack width, fluorescent resin brightness, and constituent mineral grains under polarized and ultraviolet light. The cracks were

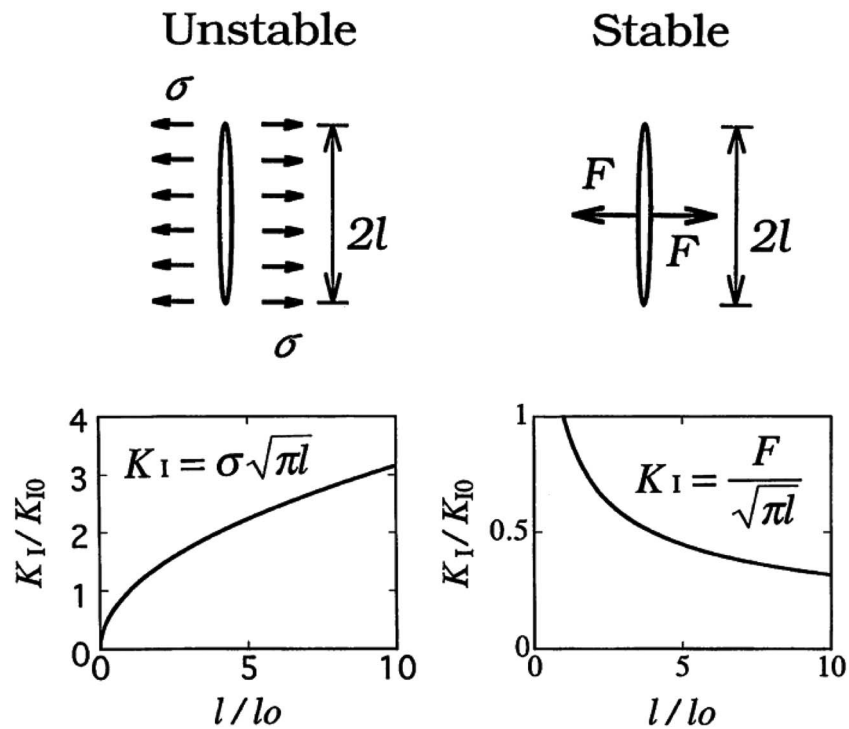


Figure 12. Stable and unstable crack growth from a viewpoint of stress intensity factor of mode I at a crack tip. (after *Ishida et al.* [1997] following *Zoback et al.* [1977] and *Zoback and Pollard* [1978].)

counted in the two opposite directions from the fracturing hole, and the number plotted is the average obtained in the both directions. Thus, the number corresponds roughly to an average number of crack branches. The number of induced cracks increased with the decrease in fluid viscosity, although the number is large for oil injection in specimen G1112. This is an exceptional case, because our observation of this specimen showed that one of the main crack propagations was obstructed by a large biotite grain near the injection hole and the crack branches were in many directions.

The trends in Figures 11e and 11f are consistent with those obtained from the AE distribution, where the average distance, L_{av} , and the fractal dimensions, FD , increased with the decrease of fluid viscosity (Figures 11b and 11c).

5. Discussion

Ishida et al. [2004] conducted HF experiments on the same kind of cubic granite as in the present study by using water and viscous oil, which showed similar crack features and fracture mechanism. *Ishida et al.* [2012], *Kizaki et al.* [2013], *Stanchits et al.* [2014], and *Bennour et al.* [2015] suggested the same dependency on the viscosity of the fracturing fluid, including SC-CO₂, based on their similar experiments using granite, tuff, sandstone, and shale. *Shimizu et al.* [2011] simulated HF using their Distinct Element Method code and provided a persuasive interpretation for the dependency of the breakdown pressure, AE fracturing mechanism, and crack features on fluid viscosity.

In actual reservoirs, *Baria and Green* [1986] in geothermal field and *Warpinski et al.* [2005] and *Dinske et al.* [2010] in tight gas reservoirs made comparative analyses of microseismicity induced by HF using viscous fluid and water. *Baria and Green* [1986] and *Dinske et al.* [2010] could not show clear difference between the two fluids, while *Warpinski et al.* [2005] showed that slickwater fracturing extends a much larger area further in three dimensions than gel fracturing, which is consistent with the findings from our laboratory experiments. In actual field operations of HF, weak planes, such as preexisting cracks, sedimentary planes and defects in strata, may behave in a similar manner to grain boundary in the granite specimens.

We concluded that HF using low-viscosity fracturing fluid tends to induce shear dominant fracture resulting in extensive three-dimensional cracking rather than the two-dimensional cracking observed for high-viscosity fluid. The three-dimensional cracks, which tend to be sinuous and have many secondary branches, could be expected to form pathways favorable for heat extraction from EGS, shale gas recovery, and other processes. In this point of view, CO₂ fracturing is better than conventional water fracturing for these purposes.

In actual field operations of HF, a solid material called proppant, typically treated sand or man-made ceramic materials, is usually injected into the induced cracks to prevent them from closing due to rock stresses. However, SC-CO₂ has little ability to transport the proppant due to its low viscosity. In addition, since CO₂ is more corrosive than water to steel pipes and other units, this nature of CO₂ may make troubles in actual HF operations. For the first problem, it may be better to inject L-CO₂, due to its larger viscosity than SC-CO₂, through a double pipe, making vacuum in a space between the inner and outer pipe to prevent it from heating underground. In another way, if we can make a new type proppant to solve into SC-CO₂ and to deposit in the cracks due to phase change of CO₂ caused by the decrease of pressure and temperature with the breakdown, the problem would be solved. For the second problem, since CO₂ injection is usually used for enhance oil recovery in the petroleum industry, the experiences would help to solve the problem.

CO₂ fracturing most likely form pathways favorable for heat extraction, and large amounts of CO₂ would remain underground distributed across many wells even if only a small amount of CO₂ is used in each well injection. Thus, by overcoming the problems for field application of this approach, CO₂ fracturing for heat extraction from EGS could realize economically viable CO₂ sequestration.

6. Conclusions

We conducted HF experiments in 170 mm cubic granite specimens with a 20 mm diameter central hole using SC-CO₂, L-CO₂, water, and viscous oil with viscosities from 0.051 to 336.6 mPas. Based on the dependency on fracturing fluid viscosity of the breakdown pressure, AE distribution, the fracturing mechanism deduced from ratios of the *P* wave first motion polarity of AE events, and crack features observed by the fluorescent method, we can draw the following conclusions.

1. The breakdown pressure increases with viscosity, which is consistent with previous experiments and numerical simulations. Thus, the breakdown pressure with the injection of a low-viscosity fluid, such as SC-CO₂, was expected to be lower than that of water, and much lower than that of viscous fluid such as gel used in field operations.
2. AE source distributions clarified that the average distance, L_{av} , from a source to the maximum likelihood plane and the fractal dimensions, *FD*, of the source distributions increased with the decrease in fluid viscosity. This suggests that HF using low-viscosity fluid tends to induce extensive three-dimensional cracking rather than the two-dimensional cracking observed for high-viscosity fluid.
3. Ratios of the *P* wave first motion polarity suggest that a low-viscosity fracturing fluid tends to induce shear dominant fracture, whereas viscous fluids tend to induce tensile dominant fracture.
4. The photomicrographs taken using a petrographic microscope in crossed-polarized light (crossed Nicols) show that the cracks induced by SC-CO₂ propagated mainly along the grain boundaries of the constituent minerals, and consequently, many small cracks inclined in the direction of the maximum compressive stress were observed. In contrast, the cracks induced by viscous oil injection cut through the many mineral grains and propagated almost straight along the direction of the maximum compressive stress without bending. Because shear stress developed on a plane inclined in the direction of the maximum compressive stress, the inclined cracks were probably induced by shear fracture. Thus, the observation was consistent with the results obtained from AE monitoring, that is, shear dominant fracturing occurred with low-viscosity fluid injection, whereas tensile dominant fracturing occurred with high-viscosity fluid injection.
5. The microscopic crack observations showed that the tortuosity of a main crack and the average number of cracks increased with the decrease in fluid viscosity. This observation was consistent with the results of AE monitoring.

6. The observed dependency of crack features on the fracturing fluid viscosity was consistent with those reported in previous laboratory experiments, numerical simulations, and with the field microseismic maps associated with the injection of water and gel.
7. These results suggest that CO₂ fracturing induces three-dimensionally sinuous cracks with many secondary branches, which seem to be desirable pathways for heat extraction from EGS, shale gas recovery, and other processes. By overcoming the difficulty in injecting proppant into induced cracks due to low viscosity of SC-CO₂, CO₂ fracturing could realize economically viable CO₂ sequestration, because large amounts of CO₂ would remain underground distributing across many wells even if only a small amount of CO₂ is used in each well injection.

Acknowledgments

In the supporting information, we show Figures S1 and S2 corresponding to Figures 7 and 8 for the alternate specimens G1202, G1209, G1103, and G1112 to confirm the generality of the properties in section 4. We also show the typical AE waveforms for respective fracturing fluids in Figure S3. The supporting information includes the Excel files used to make Figures 7 and 8 and S1 and S2. The numerical data used to make Figure 11 are shown in Table 2. This work was financially supported by the Japan Society for the Promotion of Science Grants-in-Aid for Scientific Research (B) and (A), grant 21360446 and 25249131, as well as by the ENEOS Hydrogen Trust Fund of 2012.

References

- Baria, R., and A. S. P. Green (1986), Seismicity induced during a viscous stimulation at the Camborne school of mines hot dry rock geothermal energy project in Cornwall, England, in *Progress in Acoustic Emission III*, pp. 407–429, The Jpn. Soc. of NDI, Tokyo.
- Bennour, Z., T. Ishida, Y. Nagaya, Y. Chen, Y. Nara, Q. Chen, K. Sekine, and Y. Nagano (2015), Crack extension in hydraulic fracturing of shale cores using viscous oil, water, and liquid carbon dioxide, *Rock Mech. Rock Eng.*, 48(4), 1463–1473, doi:10.1007/s00603-015-0774-2.
- Brown, D. W. (2000), A hot dry rock geothermal energy concept utilizing supercritical CO₂ instead of water, paper presented at 25th Workshop on Geothermal Reservoir Engineering, Stanford Univ., Stanford, Calif.
- Bunger, A. P., and E. Detournay (2008), Experimental validation of the tip asymptotics for a fluid-driven fracture, *J. Mech. Phys. Solids*, 56, 3101–3115.
- Bunger, A. P., A. Lakirouhani, and E. Detournay (2010), Modelling the effect of injection system compressibility and viscous fluid flow on hydraulic fracture breakdown pressure, in *Proceedings of the 5th International Symposium on In Situ Rock Stress*, pp. 59–67, Int. Soc. for Rock Mech., Beijing.
- Chen, Y., Y. Nagaya, and T. Ishida (2015), Observations of fractures induced by hydraulic fracturing in anisotropic granite, *Rock Mech. Rock Eng.*, 48, 1455–1461, doi:10.1007/s00603-015-0727-9.
- Cheung, L. S., and B. C. Haimson (1989), Laboratory study of hydraulic fracturing pressure data—How valid is their conventional interpretation?, *Int. J. Rock Mech. Min. Sci. Geomech. Abstr.*, 26, 595–604.
- Dinske, C., S. A. Shapiro, and J. T. Rutledge (2010), Interpretation of microseismicity resulting from gel and water fracturing of tight gas reservoirs, *Pure Appl. Geophys.*, 167, 169–182.
- Fenghour, A., W. A. Wakeham, and V. Vesovic (1998), The viscosity of carbon dioxide, *J. Phys. Chem. Ref. Data*, 27(1), 31–44, doi:10.1063/1.556013.
- Ge, M. (2003a), Analysis of source location algorithms—Part I: Overview and non-iterative methods, *J. Acoust. Emiss.*, 21, 21–28.
- Ge, M. (2003b), Analysis of source location algorithms—Part II: Iterative methods, *J. Acoust. Emiss.*, 21, 29–51.
- Geiger, L. (1910), Herbsetzung bei Erdbeben aus den Aukunfzeiten [German], *K. Gessell. Will. Goett.*, 4, 331–349.
- Geiger, L. (1912), Probability method for the determination of earthquake epicentres from the arrival time only, *Bull. St. Louis Univ.*, 8, 60–71.
- Grassberger, P. (1983), Generalized dimensions of strange attractors, *Phys. Lett.*, 97A(6), 227–230.
- Guo, F., N. R. Morgenstern, and J. D. Scott (1993a), An experimental investigation into hydraulic fracture propagation—Part 1. Experimental facilities, *Int. J. Rock Mech. Min. Sci. Geomech. Abstr.*, 30, 177–188.
- Guo, F., N. R. Morgenstern, and J. D. Scott (1993b), An experimental investigation into hydraulic fracture propagation—Part 2. Single well tests, *Int. J. Rock Mech. Min. Sci. Geomech. Abstr.*, 30, 189–202.
- Guo, F., N. R. Morgenstern, and J. D. Scott (1993c), An experimental study of well communication by hydraulic fracturing, *Int. J. Rock Mech. Min. Sci. Geomech. Abstr.*, 30, 203–218.
- Haimson, B., and C. Fairhurst (1969), Hydraulic fracturing in porous-permeable materials, *J. Pet. Tech.*, 21, 811–817.
- Hirata, T., T. Satoh, and K. Ito (1987), Fractal structure of spatial distribution of microfracturing in rock, *Geophys. J. R. Astron. Soc.*, 90, 369–374, doi:10.1111/j.1365-246X.1987.tb00732.x.
- International Society for Rock Mechanics, Commission on Standardization of Laboratory and Field Tests (1979), Suggested methods for determining water content, porosity, density, absorption and related properties and swelling and slake-durability index properties, *Int. J. Rock Mech. Min. Sci. Geomech. Abstr.*, 16, 143–151.
- Ishida, T., and S. Sasaki (2011), Numerical simulation to examine accuracy of AE source location and its applications to in-situ rock monitoring, *J. Acoust. Emiss.*, 29, 260–272.
- Ishida, T., K. Kitano, N. Kinoshita, and N. Wakabayashi (1990), Acoustic emission and P wave velocity monitoring during thermal cracking in a locally heated granite block [Japanese with English abstract], *J. JSCE*, 418(III-13), 153–161.
- Ishida, T., Q. Chen, and Y. Mizuta (1997), Effect of injected water on hydraulic fracturing deduced from acoustic emission monitoring, *Pure Appl. Geophys.*, 150, 627–646.
- Ishida, T., Q. Chen, H. Kaieda, and Y. Mizuta (1998), Fractal analysis on a source distribution of acoustic emissions in a hot dry rock mass reservoir [Japanese with English abstract], *J. JSCE*, 536(III-43), 49–63.
- Ishida, T., Q. Chen, Y. Mizuta, and J.-C. Roegiers (2004), Influence of fluid viscosity on the hydraulic fracturing mechanism, *J. Energy Resour. Technol.*, 126, 190–200, doi:10.1115/1.1791651.
- Ishida, T., H. Oka, N. Yonehiro, Y. Tamura, and Y. Mizuta (2005), Examination on the tensile strengths of hydraulic fracturing using the probabilistic theory of fracture [Japanese with English abstract], *J. MMIJ (Shigen-to-Sizai)*, 121, 576–582.
- Ishida, T., S. Miyazaki, T. Ishii, K. Amemiya, and Y. Mizuta (2006), Preliminary results of air permeability test under tensile stress condition using a hollow cylindrical rock specimen, in *Proceedings of EUROCK 2006*, pp. 127–131, CRC Press, Liege, Belgium.
- Ishida, T., K. Aoyagi, T. Niwa, Y. Chen, S. Murata, Q. Chen, and Y. Nakayama (2012), Acoustic emission monitoring of hydraulic fracturing laboratory experiment with supercritical and liquid CO₂, *Geophys. Res. Lett.*, 39, L16309, doi:10.1029/2012GL052788.
- Jansen, D. P., S. R. Carlson, R. P. Young, and D. A. Hutchins (1993), Ultrasonic imaging and acoustic emission monitoring of thermally induced microcracks in Lac du Bonnet granite, *J. Geophys. Res.*, 98, 22,231–22,243, doi:10.1029/93JB01816.
- Kirsch, C. (1898), Die theorie der elastizität und die bedürfnisse der festigkeitslehre [German], *Z. Ver. Dtsch. Ing.*, 42, 797–807.
- Kizaki, A., K. Ohashi, H. Tanaka, and K. Sakaguchi (2013), Effects of vertical stress on fracture propagation using supercritical carbon dioxide, in *Proceeding of EUROCK*, Int. Soc. for Rock Mech., Paper No. CH149, Wroclaw, Poland.

- Mohan, A. R., U. Turaga, V. Shembekar, D. Elsworth, and S. V. Pisupati (2013), Utilization of carbon dioxide from coal-based power plants as a heat transfer fluid for electricity generation in enhanced geothermal system (EGS), *Energy*, *57*, 505–512.
- Morita, N., A. D. Black, and G.-F. Fuh (1996), Borehole breakdown pressure with drilling fluids—1. Empirical results, *Int. J. Rock Mech. Min. Sci. Geomech. Abstr.*, *33*, 39–51.
- National Astronomical Observatory of Japan (1995), *Chronological Scientific Tables*, pp. 446–447, Maruzen, Tokyo.
- Nishiyama, T., and H. Kusuda (1994), Identification of pore spaces and micro cracks using fluorescent resins, *Int. J. Rock Mech. Min. Sci. Geomech. Abstr.*, *31*, 369–375.
- Pruess, K. (2006), Enhanced geothermal systems (EGS) using CO₂ as working fluid—A novel approach for generating renewable energy with simultaneous sequestration of carbon, *Geothermics*, *35*, 351–367.
- Rothman, R. L., R. J. Greenfield, and H. R. Hardy Jr. (1974), Errors in hypocenter location due to velocity anisotropy, *Bull. Seismol. Soc. Am.*, *64*, 1993–1996.
- Sano, O., K. Kudo, and Y. Mizuta (1992), Experimental determination of elastic constants of Oshima granite, Barre granite, and Chelmsford granite, *J. Geophys. Res.*, *97*, 3367–3379, doi:10.1029/91JB02934.
- Scheidegger, A. E. (1962), Stress in Earth's crust as determined from hydraulic fracturing data, *Geol. Bauwes.*, *27*, 45–53.
- Schmitt, D. R., and M. D. Zoback (1992), Diminished pore pressure in low-porosity crystalline rock under tensional failure: Apparent strengthening by dilatancy, *J. Geophys. Res.*, *97*, 273–288, doi:10.1029/91JB02256.
- Schmitt, D. R., and M. D. Zoback (1993), Infiltration effects in the tensile rupture of thin walled cylinders of glass and granite: Implications for the hydraulic fracturing breakdown equation, *Int. J. Rock Mech. Min. Sci. Geomech. Abstr.*, *30*, 289–303, doi:10.1016/0148-9062(93)92731-5.
- Shimizu, H., S. Murata, and T. Ishida (2011), The distinct element analysis for hydraulic fracturing in hard rock considering fluid viscosity and particle size distribution, *Int. J. Rock Mech. Min. Sci.*, *48*(5), 712–727.
- Stanchits, S., A. Surdi, P. Gathogo, E. Edelman, and R. Suarez-Rivera (2014), Onset of hydraulic fracture initiation monitored by acoustic emission and volumetric deformation measurements, *Rock Mech. Rock Eng.*, *47*, 1521–1532, doi:10.1007/s00603-014-0584-y.
- Ueda, A., K. Kato, T. Ohsumi, T. Yajima, H. Ito, H. Kaieda, R. Metcalfe, and H. Takase (2005), Experimental studies of CO₂-rock interaction at elevated temperatures under hydrothermal conditions, *Geochem. J.*, *39*, 417–425.
- Vutukuri, V. S., and K. Katsuyama (1994), *Introduction to Rock Mechanics*, pp. 125–129, Ind. & Consult, Inc., Tokyo.
- Warpinski, N. R., R. C. Kramm, J. R. Heinze, and C. K. Waltman (2005), Comparison of single- and dual-array microseismic mapping techniques in the Barnett shale, paper presented at 2005 Annual Technical Conference and Exhibition, Soc. of Pet. Eng., Dallas, Tex.
- Weibull, W. (1939a), A statistical theory of the strength of materials, *Ingeniörs Vetenskaps Akademiens, Handlingar*, 151.
- Weibull, W. (1939b), The phenomenon of rupture in solid, *Ingeniörs Vetenskaps Akademiens, Handlingar*, 153.
- Xu, C., P. Dowd, and Q. Li (2016), Carbon sequestration potential of the Habanero reservoir when carbon dioxide is used at the heat exchange fluid, *J. Rock Mech. Geotech. Eng.*, *8*, 50–59.
- Zhou, X., and T. J. Burbey (2014), Fluid effect on hydraulic fracture propagation behavior: A comparison between water and supercritical CO₂-like fluid, *Geofluids*, *14*, 174–188, doi:10.1111/gfl.12061.
- Zoback, M. D., and D. D. Pollard (1978), Hydraulic fracture propagation and the interpretation of pressure-time records for in-situ stress determination, in *Proceedings of 19th US Rock Mechanics Symposium*, pp. 14–22, Reno, Nev.
- Zoback, M. D., F. Rummel, R. Jung, and C. B. Raleigh (1977), Laboratory hydraulic fracturing experiments in intact and pre-fractured rock, *Int. J. Rock Mech. Min. Sci. Geomech. Abstr.*, *14*, 49–58.